

Ab initio theoretical study of magnetization and phase stability of the $(\text{Fe,Co,Ni})_{23}\text{B}_6$ and $(\text{Fe,Co,Ni})_{23}\text{Zr}_6$ structures of Cr_{23}C_6 and $\text{Mn}_{23}\text{Th}_6$ prototypes

P. R. Ohodnicki, Jr.,^{1,*} N. C. Cates,¹ D. E. Laughlin,¹ M. E. McHenry,¹ and M. Widom²

¹Materials Science and Engineering Department, Carnegie Mellon University, Pittsburgh, Pennsylvania 15213, USA

²Physics Department, Carnegie Mellon University, Pittsburgh, Pennsylvania 15213, USA

(Received 20 June 2008; revised manuscript received 31 August 2008; published 14 October 2008)

We present an *ab initio* theoretical investigation of the magnetization and phase stability of two different complex cubic structures of prototype Cr_{23}C_6 and $\text{Mn}_{23}\text{Th}_6$, with an emphasis on the $(\text{Fe,Co,Ni})_{23}\text{B}_6$ and $(\text{Fe,Co,Ni})_{23}\text{Zr}_6$ compositions. These phases have recently been observed as secondary or even primary crystallization products of $(\text{Fe,Co,Ni})\text{-Zr-B}$ and related metallic glasses that have been studied for applications as soft magnets with nanocrystalline grain size. We first demonstrate the validity of the theoretical technique employed through a detailed comparison between the predictions of the calculations for the Co-Zr binary system and the experimentally stable phases. We then investigate the magnetization and stability of the binary phases. While the Fe-based binary $\text{Fe}_{23}\text{Zr}_6$ and Fe_{23}B_6 phases are expected to have the highest magnetization, the Co-based binary $\text{Co}_{23}\text{Zr}_6$ and Co_{23}B_6 structures are predicted to be the most stable of each prototype. The $\text{Co}_{23}\text{Zr}_6$ structure is the only binary 23:6 structure predicted to be a stable phase for the $(\text{Fe,Co,Ni})_{23}\text{B}_6$ and $(\text{Fe,Co,Ni})_{23}\text{Zr}_6$ systems investigated here. Small additions of Zr atoms to the $(\text{Fe,Co,Ni})_{23}\text{B}_6$ phases tend to substitutionally occupy the 8c Wyckoff site and stabilize these structures. In contrast, small additions of B to the $(\text{Fe,Co,Ni})_{23}\text{Zr}_6$ phases have a much weaker site preference and tend to destabilize these structures. As a result, $(\text{Fe,Co,Ni})_{23}\text{B}_6$ structures are stabilized in $(\text{Fe,Co,Ni})\text{-Zr-B}$ systems relative to the binary $(\text{Fe,Co,Ni})_{23}\text{B}_6$ systems while the $(\text{Fe,Co,Ni})_{23}\text{Zr}_6$ phases are not. The results presented in this work are in good qualitative agreement with experimental observations of the compositional modifications tending to promote formation of the 23:6 phases in Fe-Co-Zr-B and related metallic glasses.

DOI: 10.1103/PhysRevB.78.144414

PACS number(s): 71.20.Be, 71.15.Nc, 71.20.Lp, 75.50.Bb

I. MOTIVATION AND APPROACH

Fe-, Co-, and Ni-based soft ferromagnetic nanocomposite materials are obtained by crystallizing amorphous ribbons of compositions which typically include both large (e.g., Zr or Nb) and small (e.g., B and Si) atoms relative to the ferromagnetic transition-metal elements. Examples of such compositions include the $(\text{Fe,Co,Ni})\text{-Nb-Si-B-Cu}$ -type alloys^{1,2} as well as the $(\text{Fe,Co,Ni})\text{-Zr-B}$ -type alloys.³⁻⁷ In these complex alloy systems, the large and small atoms provide good glass forming ability and they enable one to obtain a composite microstructure which consists of nanocrystals of a transition-metal rich phase embedded within an intergranular amorphous phase enriched in the glass formers after the first “primary” crystallization step.

At higher annealing temperatures resulting in so-called “secondary crystallization,” the glass-former enriched intergranular amorphous phase crystallizes as well resulting in the formation of intermetallic compounds. A number of different intermetallic compounds are noted in the literature depending on the exact alloy composition including $(\text{Fe,Co,Ni})_2\text{B}$, $(\text{Fe,Co,Ni})_2\text{Zr}$, and $(\text{Fe,Co,Ni})_3\text{B}$. More complex phases exhibiting the Cr_{23}C_6 or $\text{Mn}_{23}\text{Th}_6$ prototype structures such as $(\text{Fe,Co,Ni})_{23}\text{B}_6$ or $(\text{Fe,Co,Ni})_{23}\text{Zr}_6$ also form in a number of alloy systems. Both structures exhibit the same symmetry ($Fm\bar{3}m$ space group), Pearson symbol (cF116), and stoichiometry, but they are distinct. The Cr_{23}C_6 -type structures consist of medium-sized ferromagnetic transition-metal elements and small atoms such as B and the $\text{Mn}_{23}\text{Th}_6$ -type structures consist of medium-sized atoms and large atoms such as Zr. The former is often found as

a secondary crystallization product of high B-containing compositions,^{5,8,9} while the latter is often found for compositions which have relatively lower B contents and higher contents of Zr.^{6,7,10}

Despite the difference in the atomic radius of the second constituent elements in these intermetallic phases, both structures can be visualized in terms of an octahedral network of large ($\text{Mn}_{23}\text{Th}_6$) or small (Cr_{23}C_6) atoms as illustrated in Fig. 1. For both structures, the large or small atoms sit on the

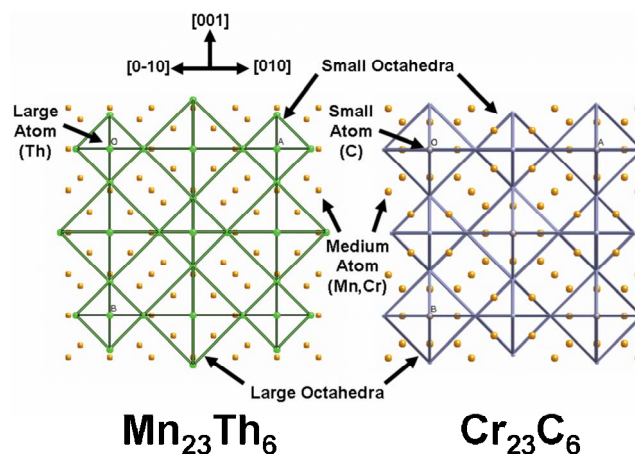


FIG. 1. (Color online) Representations of the $\text{Mn}_{23}\text{Th}_6$ and Cr_{23}C_6 prototype structures normal to the $[100]$ direction. The interconnected vertex-sharing octahedral networks of Th, large atoms, or C, small atoms, are shown. The remaining atoms are the Mn or Cr intermediate-sized transition-metal atoms. Only atoms in the first layer of the octahedral network are shown for clarity.

vertices of large and small octahedra which form an interconnected face-centered-cubic NaCl-type structure. The centers of the large octahedra form the lattice sites of a face-centered-cubic lattice and the small octahedra are then centered on the octahedral interstitial positions of the fcc lattice or vice versa. The large and small octahedra of these networks are vertex-sharing polyhedra.

The difference between the two prototype 23:6 structures lies in the decoration of the octahedral network with intermediate-sized transition-metal atoms that occupy a number of special positions. In the cases of $\text{Fe}_{23}\text{Zr}_6$ which exhibits the $\text{Mn}_{23}\text{Th}_6$ -type structure and Fe_{23}B_6 which exhibits the Cr_{23}C_6 -type structure, the special positions, fractional atomic positions, and Pearson information as listed at the online alloy database¹¹ maintained by Widom, Mikhalovic, and co-workers are presented in Fig. 2 along with graphical illustrations of the coordination of the various intermediate-sized transition-metal atom Fe sites. The 4a and 4b sites exhibit the highest symmetry in both structures and they correspond to the centers of the large octahedra of B or Zr atoms, respectively.

The 23:6 phases are not as well understood as other secondary crystallization products because they exhibit complex face-centered-cubic structures with 116 atoms per conventional unit cell and they are often metastable. In this work we develop a better understanding of the magnetization and stability of the two 23:6-type structures and the relationship between these two structures. Attention is focused on the 23:6 structures of types $(\text{Fe},\text{Co},\text{Ni})_{23}\text{B}_6$ and $(\text{Fe},\text{Co},\text{Ni})_{23}\text{Zr}_6$ because this work was motivated by the recent work in soft magnetic nanocomposites.

Ab initio density-functional theory (DFT) calculations were carried out in the spin-polarized projector-augmented wave (PAW) function approach using a generalized gradient approximation (GGA) for the exchange-correlation functional.^{12,13} The Vienna Ab-Initio Simulation Package (VASP) (Ref. 13) was employed to carry out the calculations.

Fe23B6 C6Cr23 PEARSON			
cF116 GROUPNO 225			
a=10.59496 angstroms			
psite Fe1	4a	0.000	0.000 0.000
psite Fe2	8c	0.250	0.250 0.250
psite B1	24e	0.276	0.000 0.000
psite Fe3	32f	0.381	0.381 0.381
psite Fe4	48h	0.000	0.171 0.171

Fe23Zr6 Mn23Th6 PEARSON			
cF116 GROUPNO 225			
a=11.57819 angstroms			
psite Fe1	4b	0.500	0.500 0.500
psite Fe2	24d	0.000	0.250 0.250
psite Zr1	24e	0.206	0.000 0.000
psite Fe3	32f	0.379	0.379 0.379
psite Fe4	32f	0.173	0.173 0.173

Structural relaxation and electronic structure convergence follows previously published methods.¹⁴ Unless otherwise noted, the final structural relaxation and electronic structure convergence steps were carried out with a sufficient number of k points to ensure cohesive energy convergence to less than approximately 1 meV/atom and low residual forces (<0.01 eV/Å). For both the binary and ternary 23:6-type structures, a primitive unit cell with periodic boundary conditions was used with a k -point mesh grid of at least $6 \times 6 \times 6$ in the final relaxation steps. Primitive unit cells were also used for the remaining structures, but the final k -point grid density depended upon the complexity and size of the structure.

First, we compare the results of these calculations with experimental data to discuss the validity of the theoretical framework employed here for the alloys of interest through a detailed study of the Co-Zr binary system. We then discuss predicted magnetic properties and low-temperature stability of the various binary 23:6 structures. Because the nanocomposite compositions typically include both “small” and “large” atoms, we have also investigated the effect of additions of small atoms to the stability of the $(\text{Fe},\text{Co},\text{Ni})_{23}\text{Zr}_6$ structure and large atom additions to the stability of the $(\text{Fe},\text{Co},\text{Ni})_{23}\text{B}_6$ structure. When possible, we compare the trends in stability predicted from the theoretical calculations with trends reported in relevant experimental works.

II. EXPERIMENTAL AND THEORETICAL COMPARISON: BINARY Co-Zr SYSTEM

Experimentally stable phases for the binary systems investigated were taken from the latest versions of the experimental phase diagrams presented in two separate references.^{15,16} Detailed crystal structure information was taken from the Pearson’s Handbook of Crystal Data for Intermetallic Phases.¹⁷ The equilibrium phase typically referred to as “ $\text{Co}_{11}\text{Zr}_2$ ” phase^{15,16} could not be included in calcula-

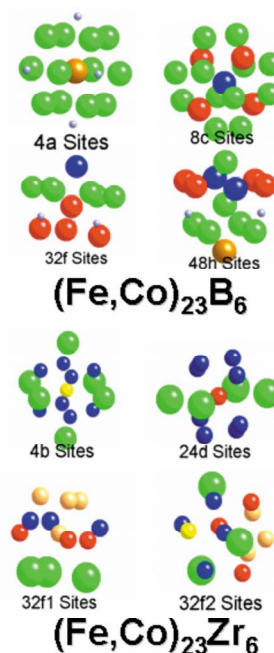


FIG. 2. (Color online) Structure information and local environments of the various intermediate-sized transition-metal sites for the Fe_{23}B_6 and $\text{Fe}_{23}\text{Zr}_6$ structures isostructural with the prototype Cr_{23}C_6 and $\text{Mn}_{23}\text{Th}_6$ structures, respectively. The values were taken from the online alloy database (Ref. 11). In the online version of the manuscript only, the atoms at different special positions are of different colors (Fe_{23}B_6 structure: orange = 4a, blue = 8c, red = 32f, green = 48h, and gray = 24e; $\text{Fe}_{23}\text{Zr}_6$ structure: yellow = 4b, red = 24d, peach = 32f1, blue = 32f2, and green = 24e). For the Fe_{23}B_6 structure, the B atoms are illustrated as small and gray. For the $\text{Fe}_{23}\text{Zr}_6$ structure, the Zr atoms are large and green.

TABLE I. Phases listed in experimental phase diagrams (Refs. 15 and 16) of the Co-Zr system. The phases calculated to be stable at $T=0$ K are shaded. Note that the CoZr_3 structure of Pearson symbol oC16 is listed as experimentally stable only in some references (e.g., compare Refs. 15 and 16).

Co-Zr Experimentally Stable Phases						
Phase	[at % Zr]	Pearson	Prototype	E_C [ev/atom]	ΔH_{mix} [kJ/mol]	ΔE [meV/atom]
FCC Co	0 to <1	cF4	Cu	-6.990	1.98	20.5
HCP Co	~0	hP2	Mg	-7.010	0.00	0.0
"Co ₁₁ Zr ₂ "	~15.5	?	?	?	?	?
Co ₂₃ Zr ₆	~20.7	cF116	Mn ₂₃ Th ₆	-7.537	-21.90	-23.3
Co ₂ Zr	~27 to <35	cF24	Cu ₂ Mg	-7.822	-31.68	-70.4
CoZr	~50	cP2	CsCl	-8.033	-28.83	1.7
CoZr ₂	~66.7	tI12	Al ₂ Cu	-8.248	-26.30	-18.0
BCC Zr	~95 to 100	cI2	W	-8.385	7.04	73.1
HCP Zr	~97.5 to 100	hP2	Mg	-8.458	0.00	0.0

Stable According to Some References						
CoZr ₃	75	oC16	Re ₃ B	-8.329	-22.44	-28.1

tions as the crystal structure and atomic positions have not yet been identified. While the *ab initio* calculations performed here only strictly provide information about the structures expected to be stable at $T=0$ K, they often provide insight into the structures which are most likely to be stable at elevated temperatures as well.

Table I lists the experimentally stable phases for the Co-Zr system. The phases predicted to be stable at low temperatures lie on the so-called convex hull of the calculated cohesive energies or enthalpies of mixing as a function of composition (see Fig. 4 for example). The convex hull is defined as the loci of the extreme values of the cohesive energies (or enthalpies of mixing) that can be obtained at a particular composition through an appropriate mixture of one or more of the phases included in the calculations. For a binary system, the convex hull therefore consists of a linear interpolation between the cohesive energies (or enthalpies of mixing) of adjacent theoretically predicted stable phases. In Table I, theoretically calculated cohesive energies (E_C), enthalpies of mixing (ΔH_{mix}), and a measure of the phase stability as compared to the other phases included in the calculations ΔE are all reported. ΔE is defined here as the difference between the cohesive energy (or enthalpy of mixing) of the phase and the convex hull calculated by excluding the phase in question.¹⁴ $\Delta E \leq 0$ therefore indicates that the phase is predicted to be stable at $T=0$ K, while $\Delta E > 0$ indicates the phase is predicted to be metastable or unstable. The magnitude of ΔE provides a quantitative estimate of the degree to which the structure is predicted to be stable or unstable relative to the other structures investigated.

The shaded structures in Table I are calculated to be stable (i.e., $\Delta E \leq 0$) with respect to the other structures included in the calculations. With the exception of the CoZr (cP2, CsCl-type) phase with a small positive value of $\Delta E = 1.7$ meV/atom, all of the low-temperature phases from the experimental phase diagrams of the Co-Zr system are calculated to be stable here as well. In Fig. 3, the calculated enthalpies of mixing of several phases are compared with two

sets of experimentally obtained values reproduced from a previous reference.¹⁸ The enthalpies calculated in this work lie between the experimental values reported previously indicating that they are in reasonably good quantitative agreement with the previous experimental results.

Once the phases from the experimental phase diagrams were investigated, we also included a number of additional hypothetical structures in the calculations. These structures include other Co-Zr phases claimed in the literature¹⁹ as well as selected structures from related alloy systems such as Ni-Zr, Fe-Zr, Co-Y, Co-Nb, Co-Ta, and Co-W.⁶ Figure 4 illustrates the theoretical enthalpies of mixing of the Co-Zr structures along with the convex hull formed by the structures predicted to be stable at $T=0$ K. Table II lists the phases predicted to be theoretically stable as well as other structures

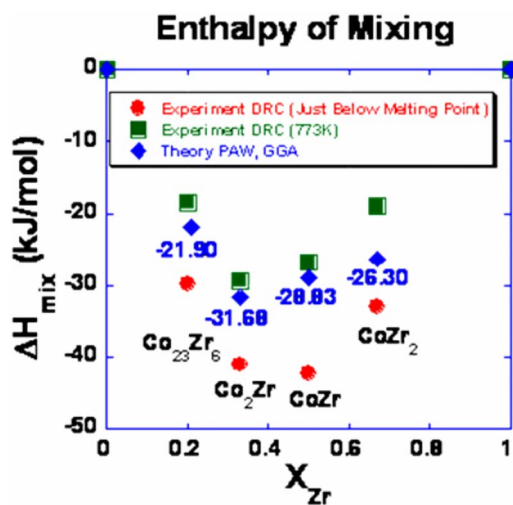


FIG. 3. (Color online) A comparison between previously measured experimental enthalpies obtained by two different sets of authors using direct reaction calorimetry (DRC) at different temperatures (Ref. 18) and theoretical enthalpies of mixing calculated here for several phases.

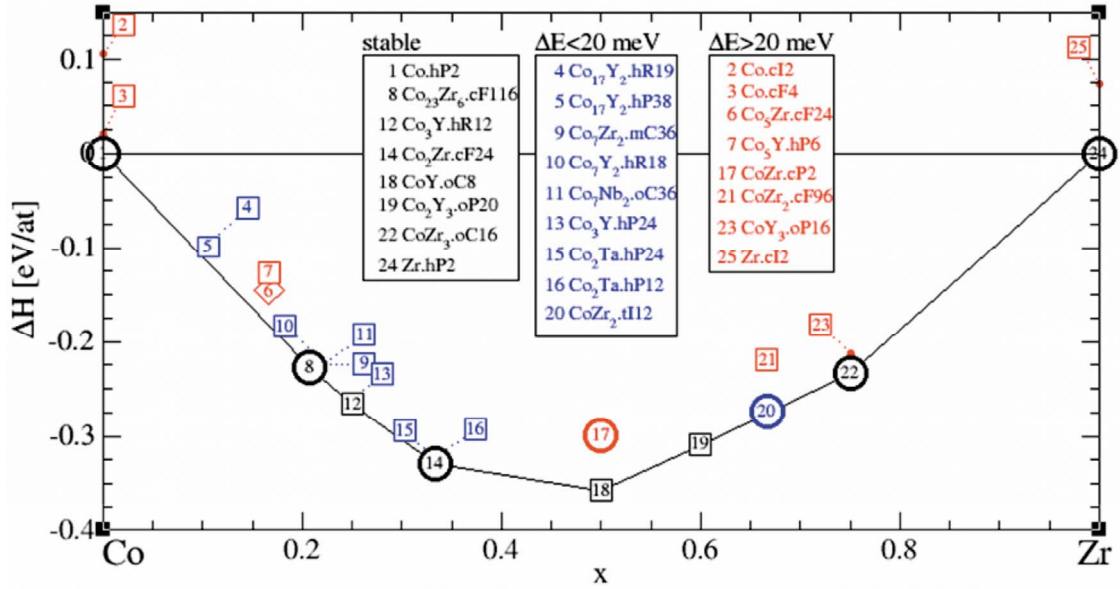


FIG. 4. (Color online) Enthalpies of mixing for the Co-Zr system with the convex hull illustrated by a solid line. The comments below regarding the color refer only to the online version of the manuscript. Circles=experimentally stable phases from Table I, black symbol =theoretically stable, blue symbol=theoretically metastable ($\Delta E < 20$ meV/atom), and red symbol=theoretically unstable ($\Delta E > 20$ meV/atom). The circles correspond to phases that are experimentally stable at low temperatures based on experimental phase diagrams (Refs. 15 and 16).

investigated with values of $\Delta E < +57.6$ meV/atom.

Figure 4 and Table II illustrate that some of the hypothetical structures investigated are more stable than or are energetically competitive with a number of the known phases from Table I. In particular, while the Co₂₃Zr₆ (cF116), Co₂Zr (cF24), and CoZr₃ (oC16) structures are predicted to be stable even after including the additional alternative structures, the CoZr (cP2) and CoZr₂ (tI12) structures are not. Instead, the lower symmetry orthorhombic Co₂Y₃ (oP20) and CoY (oC8) structures and the rhombohedral Co₃Y structure (hR12) (all with Y replaced by Zr) are predicted to be stable phases. The expected accuracy of DFT is a few meV/atom, so the ~ 58 meV/atom difference between the experimentally reported cP2 structure and our predicted oC8 structure is significant and should be pursued by further study. It is quite possible that oC8 is the true low-temperature phase. We note that the Co₂Zr₃ (oP20) structure calculated to be stable here was reported as an observed metastable phase in a previous study of crystallization of binary Co-Zr amorphous alloys by Buschow.¹⁹

Although the structure of the so-called Co₁₁Zr₂ phase is still unknown and could not be included in these calculations, Ivanova *et al.*²⁰ of an electron microscopy and x-ray diffraction study suggested that this phase actually corresponds to a high-temperature rhombohedral structure which transforms to a phase that can be indexed as an orthorhombic structure at lower temperatures. The authors suggested that these structures may be derivatives of the cubic Co₅Zr phase (cF24) which has been claimed to be a metastable phase in this system or the rhombohedral Co₃Zr phase (hR12) which is a known stable phase in the Co-Y system. While the rhombohedral Co₃Zr phase is predicted to be a stable phase at $T = 0$ K here, the Co₃Zr phase is predicted to be unstable or

metastable. There are also a number of other hexagonal and rhombohedral structures which are calculated to have relatively low positive values of ΔE (Table II).

As demonstrated here, the calculations do a reasonable job of reproducing the experimental phase diagram of the Co-Zr system if only experimentally observed phases are included. However, more extensive calculations including a number of additional phases predict that a number of additional hypothetical structures should be stable in this system as well. Some disagreements between the theoretical and experimental phase diagrams indicate the need for further study while others lie within the uncertainty of our calculation method. Because we are interested here in the stability with respect to the experimentally observed phases, only the known stable phases from experimental phase diagrams^{15,16} (Table I) were included in the calculations discussed in the remainder of this work. The other binary systems of interest were treated in the same way except that we have also included the corresponding metastable or unstable 23:6 phases for these systems. The general agreement between the experimental phase diagram and the theoretical calculations for these systems is similar to the Co-Zr system discussed in detail above. For completeness, we present a brief comparison between the theoretical calculations carried out here and the phases taken from the experimental phase diagrams for each system in the Appendix.

III. BINARY (Fe,Co,Ni)₂₃Zr₆ AND (Fe,Co,Ni)₂₃B₆ STRUCTURES

Table III illustrates results of calculations carried out for the binary (Fe,Co,Ni)-Zr and (Fe,Co,Ni)-B systems including the relative stability (ΔE), the cohesive energy (E_C), the

TABLE II. Theoretically stable phases and selected ($\Delta E < 57.6$ meV/atom) theoretically unstable/metastable phases for the Co-Zr system. The theoretically stable phases are shaded and the reference numbers for Fig. 4 are presented in the column labeled #.

Co-Zr Theoretically Stable Phases

Phase	(at % Zr)	Pearson	Prototype	E_c (ev/atom)	ΔH_{mix} (kJ/mol)	ΔE (meV/atom)	#
HCP Co	0	hP2	Mg	-7.010	0.00	0.0	1
Co ₂₃ Zr ₆	20.7	cF116	Mn ₂₃ Th ₆	-7.537	-21.90	-7.1	8
Co ₃ Zr	16.7	hR12	Be ₃ Nb	-7.638	-25.64	-2.4	12
Co ₂ Zr	33.3	cF24	Cu ₂ Mg	-7.822	-31.68	-0.1	14
CoZr	50	oC8	BCr	-8.091	-34.38	-40.3	18
Co ₂ Zr ₃	60	oP20	Co ₂ Y ₃	-8.188	-29.78	-1.9	19
CoZr ₃	75	oC16	Re ₃ B	-8.329	-22.44	-20.8	22
HCP Zr	100	hP2	Mg	-8.458	0.00	0.0	24

Other Selected Structures ($\Delta E < 57.6$ meV/atom)

Phase	(at % Zr)	Pearson	Prototype	E_c (ev/atom)	ΔH_{mix} (kJ/mol)	ΔE (meV/atom)	#
CoZr ₂	66.7	tI12	Al ₂ Cu	-8.248	-26.30	2.2	20
Co ₃ Zr	25	hP24	CeNi ₃	-7.636	-25.41	2.4	13
Co ₂ Zr	33.3	hP24	MgNi ₂	-7.817	-31.23	4.7	15
Co ₂ Zr	33.3	hP12	MgZn ₂	-7.816	-31.10	6.0	16
Co ₁₇ Zr ₂	10.5	hP38	Ni ₁₇ Th ₂	-7.261	-9.52	16.9	5
Co ₇ Zr ₂	22.2	mC36	Ni ₇ Zr ₂	-7.556	-21.56	17.4	9
Co ₇ Zr ₂	22.2	hR18	Co ₇ Er ₂	-7.555	-21.50	18.0	10
Co ₁₇ Zr ₂	10.5	hR19	Th ₂ Zn ₁₇	-7.260	-9.36	18.5	4
Co ₇ Zr ₂	22.2	oC36	Co ₇ Nb ₂	-7.554	-21.43	18.7	11
CoZr ₃	75	oP16	CFe ₃	-8.308	-20.44	20.8	23
Co ₅ Zr	16.7	cF24	AuBe ₅	-7.397	-14.03	37.5	6
CoZr ₂	66.7	cF96	NiTl ₂	-8.195	-21.16	55.6	21
Co ₅ Zr	16.7	hP6	CaCu ₅	-7.377	-12.13	57.3	7
CoZr	50	cP2	CsCl	-8.033	-28.83	57.6	17

enthalpy of mixing (ΔH_{mix}), the lattice parameter (a), the net magnetization (M), and the average moment per atom (μ) for all of the 23:6 phases. The calculated lattice parameters differ from those assumed in a previous theoretical treatment.⁵ Only the binary Co₂₃Zr₆ phase is predicted to be low-temperature stable which (with the exception of the Fe₂₃Zr₆ structure) is consistent with the experimental phase

diagrams for the corresponding binary systems (Table I and Appendix). The Co₂₃B₆ structure is predicted to be the most stable of all of the metastable (Fe,Co,Ni)₂₃B₆-type structures. In addition, the largest positive values of ΔE are observed for the Ni₂₃Zr₆ (+43.9 meV/atom) and Ni₂₃B₆ (+20.7 meV/atom) structures indicating that they are least stable in the Ni-Zr and Ni-B systems.

TABLE III. Relevant results of calculations from binary (Fe,Co,Ni)-Zr and (Fe,Co,Ni)-B systems for the corresponding cubic 23:6-type structures. E_c is the cohesive energy, ΔH_{mix} is the enthalpy of mixing, ΔE is the relative stability of the structure as compared to the known experimentally stable phases, a is the lattice parameter, M is the magnetization, and μ is the net moment per atom in units of μ_B . The shaded structure is predicted to be theoretically stable ($\Delta E < 0$).

Results of Calculations for Binary 23:6 Phases

Phase	E_c (ev/atom)	ΔH_{mix} (kJ/mol)	ΔE (meV/atom)	a (Å)	M (emu/cc)	μ (μ_B)
Fe ₂₃ Zr ₆	-8.430	-16.65	7.9	11.578	990	1.42
Co ₂₃ Zr ₆	-7.537	-21.90	-23.3	11.426	634	0.88
Ni ₂₃ Zr ₆	-6.449	-35.69	43.9	11.432	0	0.00
Fe ₂₃ B ₆	-8.062	-16.49	18.6	10.595	1497	1.65
Co ₂₃ B ₆	-7.095	-14.63	9.1	10.415	923	0.97
Ni ₂₃ B ₆	-5.915	-19.47	20.7	10.447	75	0.08

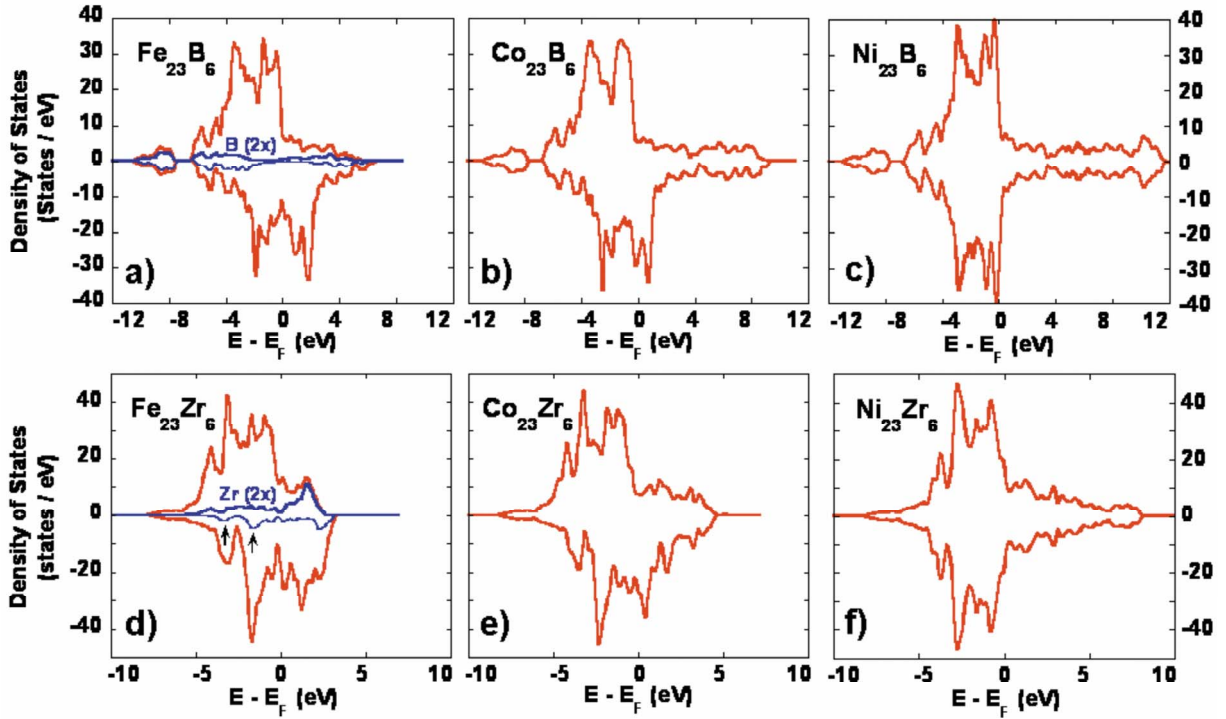


FIG. 5. (Color online) Theoretical total majority (positive) and minority (negative) spin band independent electron densities of states per f.u. for the (a) Fe_{23}B_6 , (b) Co_{23}B_6 , (c) Ni_{23}B_6 , (d) $\text{Fe}_{23}\text{Zr}_6$, (e) $\text{Co}_{23}\text{Zr}_6$, and (f) $\text{Ni}_{23}\text{Zr}_6$ structures. All energies are measured with respect to the Fermi energy (E_F). For the Fe_{23}B_6 and $\text{Fe}_{23}\text{Zr}_6$ structures, the local densities of states (multiplied by a factor of 2 for clarity) for the B and Zr atoms are also illustrated. The arrows indicate approximate energies where the minority band of Zr shows enhancements in amplitude resulting in a net negative moment at each site.

From Table III, the net magnetic moments of both types of 23:6 phases are predicted to be largest for the Fe-based phases and smallest for the Ni-based phases. In addition, the B-based structures have significantly higher magnetization than the Zr-based structures. These trends are shown graphically (Fig. 5) in the density of states for each structure with the energies measured relative to the Fermi energy. For the $\text{Fe}_{23}\text{Zr}_6$ and Fe_{23}B_6 phases, the local densities of states for the Zr and B atoms are illustrated as well. Based on Fig. 5, there is no clear exchange splitting of the majority- and minority-spin bands for the Ni-based structures which explains the suppressed magnetism of Ni atoms. Calculations for hypothetical nonmagnetic $(\text{Fe},\text{Co},\text{Ni})_{23}\text{Zr}_6$ and $(\text{Fe},\text{Co},\text{Ni})_{23}\text{B}_6$ structures suggest that the Ni-based structures have the lowest values of the density of states at the Fermi level because the Ni d -band is almost completely filled in both structures. According to the well-known Stoner criterion,²¹ a reduced density of states at the Fermi level could result in a diminished tendency toward spontaneous exchange splitting between the majority- and minority-spin bands.

Because the ferromagnetic transition-metal elements occupy four different types of special positions in the cubic 23:6 structures with unique symmetries and neighboring atomic configurations, an effective localized moment can be attributed to each type of site. In order to do this, a Voronoi polyhedron analysis²² was performed and the spatially dependent spin-polarized electron density was integrated within each Voronoi cell. The results of the Voronoi analysis

are presented in Table IV including the multiplicity of each site and the number of faces, polyhedron type, volume, and integrated spin polarization of the associated Voronoi polyhedron. The polyhedron is presented according to the convention (F_3, F_4, F_5, \dots) , where F_N is the number of faces of the Voronoi polyhedron with N edges.

For both structures, the Fe atoms tend to have the largest local moments and the local moments of all of the Ni atoms are reduced or even completely suppressed as compared to the calculated value for pure fcc Ni. Not surprisingly, the local moments vary significantly for ferromagnetic transition-metal elements at different sites in each structure.

It is difficult to provide qualitative arguments rationalizing the local atomic environment at each site and the estimated local moments. However, in the case of the Zr-type structure, the largest local moment is observed for the $4b$ sites that have a local bcc-type nearest-neighbor coordination of ferromagnetic transition-metal elements with an interatomic near-neighbor distance similar to that predicted for bcc Fe and Co (Fig. 2). The similarity between the local moments at the $4b$ sites of $2.26\mu_B$ for Fe and $1.83\mu_B$ for Co with that calculated using the same technique for bcc Fe ($2.17\mu_B$) and bcc Co ($1.71\mu_B$) indicates that the local atomic environment dictates the local moment at each site in this complex structure.

In the case of the B-type structure, the largest local moments are observed at the $4a$ and $8c$ sites. As has been pointed out previously in theoretical calculations for the $(\text{Fe},\text{Co})_{23}\text{B}_6$ structures,⁵ large local moments are observed

TABLE IV. Voronoi analysis of the different sites of the binary (Fe,Co,Ni)-Zr (a) and (Fe,Co,Ni)-B (b) cubic 23:6-type structures. The atomic diameters of the relevant elements are listed as well for reference.

a) (Fe,Co,Ni) ₂₃ Zr ₆ Zr, D=3.18Å			
	Multiplicity	# Faces	Polyhedron Type
4b	1	14	(0,6,0,8)
24d	6	12	(0,0,12)
Zr 24e	6	17	(0,1,12,4)
32f1	8	13	(0,3,6,4)
32f2	8	12	(0,0,12)

b) (Fe,Co,Ni) ₂₃ B ₆ B, D=1.80Å			
	Multiplicity	# Faces	Polyhedron Type
4a	1	18	(0,6,0,12)
8c	2	16	(0,0,12,4)
B 24e	6	9	(0,5,4)
32f	8	13	(0,3,6,4)
48h	12	14	(0,0,12,2)

	V (angst ³)	μ_{local} (μ_B)	Transition Metal
4b	11.52	2.26	Fe ₂₃ Zr ₆ Fe, D=2.48Å
24d	10.63	1.67	
Zr 24e	22.44	-0.49	
32f1	11.35	2.20	
32f2	10.57	1.79	
4b	10.86	1.83	Co ₂₃ Zr ₆ Co, D=2.51Å
24d	10.36	1.30	
Zr 24e	21.89	-0.38	
32f1	10.84	1.17	
32f2	10.22	1.11	
4b	10.73	0.00	Ni ₂₃ Zr ₆ Ni, D=2.49Å
24d	10.3	0.00	
Zr 24e	21.78	0.00	
32f1	10.8	0.00	
32f2	10.48	0.00	

	V (angst ³)	μ_{local} (μ_B)	Transition Metal
4a	11.88	2.64	Fe ₂₃ B ₆ Fe, D=2.48Å
8c	12.99	2.60	
B 24e	4.7	-0.19	
32f	11.45	1.90	
48h	11.55	2.16	
4a	10.83	1.59	Co ₂₃ B ₆ Co, D=2.51Å
8c	12.4	1.91	
B 24e	4.4	-0.13	
32f	11.06	0.99	
48h	10.99	1.30	
4a	11.06	0.26	Ni ₂₃ B ₆ Ni, D=2.49Å
8c	12.65	0.43	
B 24e	4.45	0.00	
32f	11.13	0.06	
48h	11.08	0.07	

for some of the transition-metal atoms at these sites (Fe 4b = 2.64 μ_B , Fe 8c = 2.60 μ_B , Co 8c = 1.91 μ_B) relative to those calculated for pure bcc Fe (2.17 μ_B) and fcc Co (1.60 μ_B). Bagayoko and Callaway²³ suggested that the large local moments in the Fe-based alloy are a result of the large volumes associated with these sites resulting in localization of the *d* states and an enhancement in the moment toward that expected for atomic Fe.

In the Fe- and Co-based 23:6 structures, both the B and Zr atoms are estimated to have small negative local moments. This result is in agreement with previous theoretical calculations⁵ and is typically observed for alloys of ferromagnetic transition-metal elements with early transition metals such as Zr as discussed by O’Handley.²¹ For the Fe₂₃Zr₆ and Fe₂₃B₆ structures, the negative local moments of both the Zr and B sites are associated with enhancements in the amplitude of the minority spin band density of states below the Fermi level. This is most clearly observed for the Zr atoms of the Fe₂₃Zr₆ structure as indicated by arrows in Fig. 5(d).

In a number of references in the literature,²⁴ what is presumably the (Fe, Co, Ni)₂₃Zr₆ phase has also been referred to using the stoichiometric formula (Fe, Co, Ni)₃Zr. Based on the multiplicity of the special positions listed in Table IV, there is no way of replacing all of the ferromagnetic transition-metal elements at a single site with Zr in order to obtain a structure of this stoichiometry. To investigate this possibility further, direct substitution of Co atoms with additional Zr in the Co₂₃Zr₆ structure was attempted to investigate the effects on the predicted stability. For substitution of one Co with Zr per f.u. bringing the stoichiometry closest to Co₃Zr at Co₂₂Zr₇, the corresponding values of ΔE obtained are 15.2, 53.4, 48.8, and 73.5 meV/atom for placement of Zr

at the 4b, 24d, 32f1, and 32f2 sites, respectively. In all of these cases, the substitution destabilizes the structure which is consistent with the line compound nature of the Co₂₃Zr₆ intermetallic phase. As a result, a stable structure of approximate stoichiometry Co₃Zr based on the prototype Mn₂₃Th₆ structure could not be identified here. The conclusions are the same for the corresponding Fe₂₃Zr₆ structure and it is actually predicted to be destabilized even more strongly by Zr substitutions.

As can be observed in Table IV, the 8c site of the (Fe,Co,Ni)₂₃B₆ structure is unique as the Voronoi polyhedron has a much larger volume associated with it than the remaining sites.²⁵ Because of the large volume associated with the 8c site, the theoretical treatment demonstrated a strong tendency for large atoms such as Nb and Zr to preferentially occupy it thereby stabilizing the (Fe,Nb)₂₃B₆ and (Fe,Zr)₂₃B₆ structures relative to the binary Fe₂₃B₆ phase.²⁵ If all of the 8c sites are occupied by Nb atoms, a structure of stoichiometry Fe₂₁Nb₂B₆ would be expected. Experimental results are consistent with these predictions. For example, 23:6 phase crystals of approximate composition (Fe,Co)₂₁Nb₂B₆ have been observed experimentally in complex nanocomposite alloys after secondary crystallization^{8,9} and a crystalline phase of the “Fe₂₃B₆-type” structure was found only in Nb-containing alloys.²⁶

A corresponding theoretical study of the effects of small atom additions to the (Fe,Co,Ni)₂₃Zr₆ structures has not been carried out previously despite the relevance to the soft magnetic nanocomposite alloys discussed above. Because of the small size of these atoms, interstitial incorporation rather than substitutional incorporation may actually be favored. Based on Table IV, there is not a single site in the (Fe,Co,Ni)₂₃Zr₆ structure with a dramatically different vol-

TABLE V. Cohesive energy (E_c), enthalpy of mixing (ΔH_{mix}), and relative stability (ΔE) for a number of Zr incorporations into the $(\text{Fe,Co,Ni})_{23}\text{B}_6$ structures. The 8c incorporations are the most favorable and they actually stabilize the structure relative to the Zr-free structure. The structures predicted to be stable ($\Delta E \leq 0$) are shaded.

Stoichiometry	Zr Site	Type	E_c (eV/atom)	ΔH_{mix} (kJ/mol)	ΔE (meV/atom)
Fe_{23}B_6	N/A	None	-8.062	-16.5	18.6
$\text{B}_5\text{Fe}_{22}\text{Zr}_1$	4a	Zr for Fe	-8.092	-18.60	36.2
$\text{B}_5\text{Fe}_{22}\text{Zr}_1$	8c	Zr for Fe	-8.120	-21.28	8.4
$\text{B}_5\text{Fe}_{22}\text{Zr}_1$	32f	Zr for Fe	-8.047	-14.12	82.7
$\text{B}_5\text{Fe}_{22}\text{Zr}_1$	48h	Zr for Fe	-8.060	-15.43	69.1
$\text{B}_5\text{Fe}_{21}\text{Zr}_2$	8c	Zr for all Fe	-8.168	-25.04	8.8
$\text{B}_5\text{Fe}_{20}\text{Zr}_3$	8c, 4a	Zr for all Fe	-8.204	-27.67	21.0

Stoichiometry	Zr Site	Type	E_c (eV/atom)	ΔH_{mix} (kJ/mol)	ΔE (meV/atom)
Co_{23}B_6	N/A	None	-7.095	-14.63	9.1
$\text{B}_5\text{Co}_{22}\text{Zr}_1$	4a	Zr for Co	-7.152	-15.30	65.8
$\text{B}_5\text{Co}_{22}\text{Zr}_1$	8c	Zr for Co	-7.218	-21.63	-1.6
$\text{B}_5\text{Co}_{22}\text{Zr}_1$	32f	Zr for Co	-7.124	-12.65	93.3
$\text{B}_5\text{Co}_{22}\text{Zr}_1$	48h	Zr for Co	-7.137	-13.83	81.0
$\text{B}_5\text{Co}_{21}\text{Zr}_2$	8c	Zr for all Co	-7.328	-27.45	-16.7
$\text{B}_5\text{Co}_{20}\text{Zr}_3$	8c, 4a	Zr for all Co	-7.405	-30.04	8.2
$\text{B}_5\text{Co}_{23}\text{Zr}_1$	24d	Zr for B	-7.087	-7.97	114.6
$\text{Co}_{23}\text{Zr}_6$	24d	Zr for all B	-6.912	38.30	625.0

Stoichiometry	Zr Site	Type	E_c (eV/atom)	ΔH_{mix} (kJ/mol)	ΔE (meV/atom)
Ni_{23}B_6	N/A	None	-5.915	-19.47	20.7
$\text{B}_5\text{Ni}_{22}\text{Zr}_1$	4a	Zr for Ni	-6.070	-24.51	50.3
$\text{B}_5\text{Ni}_{22}\text{Zr}_1$	8c	Zr for Ni	-6.115	-28.80	5.8
$\text{B}_5\text{Ni}_{22}\text{Zr}_1$	32f	Zr for Ni	-6.031	-20.71	89.8
$\text{B}_5\text{Ni}_{22}\text{Zr}_1$	48h	Zr for Ni	-6.040	-21.55	81.0
$\text{B}_5\text{Ni}_{21}\text{Zr}_2$	8c	Zr for all Ni	-6.306	-37.25	-17.0
$\text{B}_5\text{Ni}_{20}\text{Zr}_3$	8c, 4a	Zr for all Ni	-6.463	-42.47	-11.5

ume that is analogous to the 8c site of the $(\text{Fe,Co,Ni})_{23}\text{B}_6$ structures. It is therefore not clear what the most favorable site for small atom additions such as B should be in these complex structures.

In the remainder of this work, we extend the theoretical investigation of the effects of incorporating “large atoms” into the $(\text{Fe,Co,Ni})_{23}\text{B}_6$ structure and we perform a corresponding investigation for incorporation of “small atoms” into the $(\text{Fe,Co,Ni})_{23}\text{Zr}_6$ structure. Unless otherwise noted in the subsequent calculations, all ΔE values presented were calculated by including all of the ternary incorporations discussed in the following sections (Secs. IV–VI) but without considering any other possible ternary phases. The ΔE values presented in the remainder of this manuscript therefore only provide information about the relative stability of the Zr-substituted and B-substituted 23:6 structures in the case where other possible ternary (Fe,Co,Ni) -Zr-B compounds are kinetically prohibited from forming.

IV. TERNARY ADDITIONS OF Zr TO THE $(\text{Fe,Co,Ni})_{23}\text{B}_6$ STRUCTURES

As discussed in Sec. III, the substitutional incorporation of Zr into the Fe_{23}B_6 structure has been investigated theoretically.²⁵ In Table V, we present results of substitutional incorporations of one, two, and three Zr atoms per primitive cell for all of the $(\text{Fe,Co,Ni})_{23}\text{B}_6$ structures. A strongly favored 8c substitution is observed with $\Delta E < 0$ (Co_{23}B_6 and Ni_{23}B_6) or a reduced value of $\Delta E > 0$ (Fe_{23}B_6) as compared to the Zr-free B-type 23:6 phases indicating these additions stabilize them relative to all of the corresponding binary structures. Incorporation of Zr at sites other than 8c results in a destabilization of the $(\text{Fe,Co,Ni})_{23}\text{B}_6$ structure indicating a strong site preference for Zr atoms to occupy the 8c site.

It is interesting to point out that recent work⁵ has found that the $(\text{Fe,Ni})_{23}\text{B}_6$ phase can be obtained as the primary crystallization product in high Ni-containing Fe-Ni-Zr-B

TABLE VI. Cohesive energy (E_C), enthalpy of mixing (ΔH_{mix}), and relative stability (ΔE) for a number of B incorporations into the (Fe,Co,Ni)₂₃Zr₆ structures. The only structure predicted to be stable is the binary Co₂₃Zr₆ structure which is shaded.

Stoichiometry	B Site	Type	E_C (eV/atom)	ΔH_{mix} (kJ/mol)	ΔE (meV/atom)
Fe ₂₃ Zr ₆	N/A	None	-8.430	-16.65	7.9
B ₁ Fe ₂₃ Zr ₆	4a (D,D,D)	Interstitial	-8.362	-15.11	53.0
B ₁ Fe ₂₂ Zr ₆	4b	B for Fe	-8.392	-18.08	29.5
B ₁ Fe ₂₂ Zr ₆	24d	B for Fe	-8.388	-17.67	33.7
B ₁ Fe ₂₂ Zr ₆	32f1	B for Fe	-8.37	-16.03	50.8
B ₁ Fe ₂₂ Zr ₆	32f2	B for Fe	-8.393	-18.13	29.0
B ₄ Fe ₁₉ Zr ₆	24d	B for all Fe	-8.171	-21.97	170.8
B ₈ Fe ₁₅ Zr ₆	32f1	B for all Fe	-8.058	-21.20	251.4
B ₈ Fe ₁₅ Zr ₆	32f2	B for all Fe	-8.076	-22.88	233.9

Stoichiometry	B Site	Type	E_C (eV/atom)	ΔH_{mix} (kJ/mol)	ΔE (meV/atom)
Co ₂₃ Zr ₆	N/A	None	-7.537	-21.90	-23.3
B ₁ Co ₂₃ Zr ₆	4a (D,D,D)	Interstitial	-7.533	-23.50	8.30
B ₁ Co ₂₂ Zr ₆	4b	B for Co	-7.534	-22.73	24.40
B ₁ Co ₂₂ Zr ₆	24d	B for Co	-7.544	-23.62	15.20
B ₁ Co ₂₂ Zr ₆	32f1	B for Co	-7.515	-20.85	43.90
B ₁ Co ₂₂ Zr ₆	32f2	B for Co	-7.528	-22.09	31.10
B ₁ Co ₂₃ Zr ₅	24e	B for Zr	-7.361	-10.86	111.60
B ₄ Co ₁₉ Zr ₆	24d	B for all Zr	-7.533	-27.96	135.00
B ₈ Co ₁₅ Zr ₆	32f1	B for all Zr	-7.443	-21.47	268.40
B ₈ Co ₁₅ Zr ₆	32f2	B for all Zr	-7.423	-19.50	288.80
B ₆ Co ₂₃	24e	B for all Zr	-6.714	22.08	390.20

Stoichiometry	B Site	Type	E_C (eV/atom)	ΔH_{mix} (kJ/mol)	ΔE (meV/atom)
Ni ₂₃ Zr ₆	N/A	None	-6.449	-35.70	43.9
B ₁ Ni ₂₃ Zr ₆	4a (D,D,D)	Interstitial	-6.478	-36.46	60.40
B ₁ Ni ₂₂ Zr ₆	4b	B for Ni	-6.516	-38.02	55.20
B ₁ Ni ₂₂ Zr ₆	24d	B for Ni	-6.508	-37.21	63.60
B ₁ Ni ₂₂ Zr ₆	32f1	B for Ni	-6.703	-36.24	77.30
B ₁ Ni ₂₂ Zr ₆	32f2	B for Ni	-6.492	-35.69	79.40
B ₄ Ni ₁₉ Zr ₆	24d	B for all Ni	-6.689	-34.31	204.80
B ₈ Ni ₁₅ Zr ₆	32f1	B for all Ni	-6.703	-27.47	318.70
B ₈ Ni ₁₅ Zr ₆	32f2	B for all Ni	-6.692	-26.40	329.90

amorphous alloys even though the binary phase is expected to be metastable in both the Fe-B and Ni-B systems. Similarly, a stronger tendency to form the (Fe,Ni)₂₃B₆ structure during crystallization of Ni-containing or Ni-rich (Fe,Ni)-Zr-B alloys has been reported.²⁷ Based on the results of Table V, we propose that these observations are due to Zr incorporations that tend to stabilize the Ni-based structure more effectively than the Fe-based structure. In general, the presence of large atoms such as Zr and Nb in nanocomposite forming compositions will tend to stabilize the (Fe,Co,Ni)₂₃B₆-type phases as crystallization products in these materials as compared to the metastable Nb and Zr-free (Fe,Co,Ni)₂₃B₆ phases.

To illustrate that the (Fe,Co,Ni)₂₃B₆ structures are indeed distinct structures, we investigated the stability of the Co₂₃B₆ structure with one or all of the B atoms per primitive cell substituted by Zr. The results are included in Table V and in both cases; direct substitution of B with Zr is highly unfavorable as indicated by the large positive values of ΔE . This direct substitution was implied in a discussion of recent experimental work on crystallization of amorphous Co-Zr-B alloys²⁸ in which the chemical formula of Co₂₃(B,Zr)₆ was presented. Based on our results, this assumed chemical formula is not correct. The difference in the special positions occupied by Co atoms in the Co₂₃B₆ and Co₂₃Zr₆ structures makes them unique and the large size difference between B

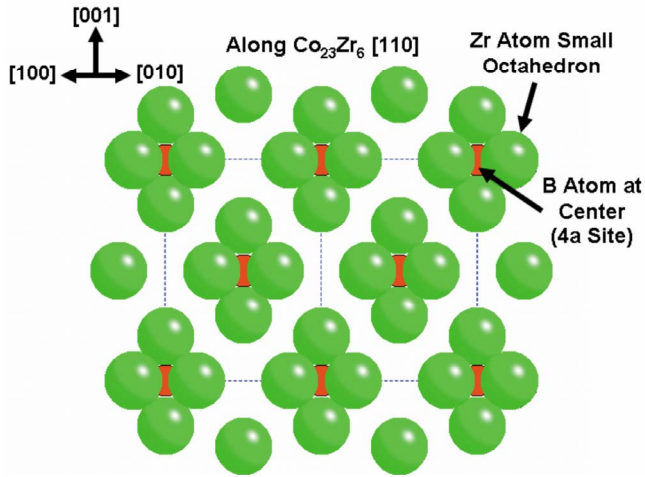


FIG. 6. (Color online) [110]-type projection of the $B_1Co_{23}Zr_6$ structure predicted to be the least unfavorable way to incorporate one B atom per primitive cell of the $Co_{23}Zr_6$ structure. The B atoms are located at the largest interstitial site in the structure. For clarity, the Co atoms are not shown.

and Zr atoms makes direct substitution in these structures energetically unfavorable.

V. TERNARY ADDITIONS OF B TO THE $(Fe, Co, Ni)_{23}Zr_6$ STRUCTURES

Because B is very small relative to Fe, Co, Ni, and Zr, the possibility of interstitial incorporation must be considered for incorporation into the $(Fe, Co, Ni)_{23}Zr_6$ structures. The largest interstitial sites were identified as a $4a$ site located at $(0,0,0)$ in the 116 atom conventional cubic unit cell using an algorithm that searches for the empty site with the largest minimum distance to the nearest-neighbor atom, d . The $4a$ interstitial site in this structure is located at the center of the small octahedra formed by the Zr atoms. For the $Co_{23}Zr_6$ structure, the $4a$ site exhibits a minimum distance to a near-neighbor atom of $d=2.41$ Å which is slightly larger than the corresponding distance ($d=2.35$ Å) in the $Co_{23}B_6$ structure. The next largest interstitial site was found to be a high multiplicity site with $d=1.79$ Å which is far too small.

We attempted a series of substitutional and interstitial B additions to $(Fe, Co, Ni)_{23}Zr_6$ and the associated values of ΔE are listed in Table VI. First, we incorporated one B atom per primitive cell corresponding to stoichiometries of $B_1(Fe, Co, Ni)_{22}Zr_6$ or $B_1(Fe, Co, Ni)_{23}Zr_5$ for substitutional additions and $B_1(Fe, Co, Ni)_{23}Zr_6$ for interstitial incorporation. For completeness, substitution of all of the (Fe, Co, Ni) atoms with B was then attempted at each site as well as substitution of all of the Zr atoms with B for the $Co_{23}Zr_6$ structure. The ΔE values listed in Table VI indicate that none of the B incorporations tend to further stabilize the $(Fe, Co, Ni)_{23}Zr_6$ structures. For the $Co_{23}Zr_6$ structure predicted to be stable in the binary system, one B addition at any of the sites results in an unstable structure. In some cases, the enthalpy of mixing (ΔH_{mix}) does become more negative for the B-incorporated $(Fe, Co, Ni)_{23}Zr_6$ structures

even though the corresponding ΔE is increased. As a result, these B-incorporated structures could potentially be observed as metastable phases although B incorporations do not stabilize the structures relative to other possible phases in this system. These results indicate that, unlike Zr incorporation into the $(Fe, Co, Ni)_{23}B_6$ structures, B incorporations into the $(Fe, Co, Ni)_{23}Zr_6$ structures tend to destabilize them.

The results of Table VI also indicate that there is no clearly preferred site for the incorporation of a small amount of B into the structure. In the case of the $Co_{23}Zr_6$ structure, interstitial incorporation of B at the $4a$ site ($\Delta E = 15.10$ meV/atom) is the least unfavorable and the resultant structure consisting of the $Co_{23}Zr_6$ structure with all of the small Zr-octahedron centers occupied by B is illustrated graphically in Fig. 6. In the case of the $Fe_{23}Zr_6$ and $Ni_{23}Zr_6$ structures, substitutions of B for Fe at the $32f2$ ($\Delta E = 29.1$ meV/atom) or $4b$ ($\Delta E = 29.5$ meV/atom) sites and Ni at the $4b$ sites ($\Delta E = 55.2$ meV/atom) are the least unfavorable. Even for a given structure, the ΔE values can be quite similar for different types of B incorporations and so it is possible that the B atoms could be incorporated both interstitially at the $4a$ sites and substitutionally at several different ferromagnetic transition-metal sites.

VI. $(Fe, Co, Ni)_{23}B_6$ AND $(Fe, Co, Ni)_{23}Zr_6$ STRUCTURES WITH MULTIPLE FERROMAGNETIC ELEMENTS (Fe, Co, AND Ni)

The similar atomic sizes of the Fe, Co, and Ni atoms result in the possibility of complete solubility in the structures which they form. As a result, it would be computationally intensive to comprehensively investigate the stability of the general ternary and quaternary $(Fe, Co, Ni)_{23}Zr_6$ and $(Fe, Co, Ni)_{23}B_6$ compositions such as $(Fe_{0.5}Co_{0.5})_{23}Zr_6$ and a thorough systematic study was not performed here. Nevertheless, it is possible that a ternary or quaternary composition with multiple ferromagnetic transition-metal elements may be relatively more stable than either of the corresponding binary 23:6 phases because of the multiple possible sites for the ferromagnetic transition-metal elements with unique atomic environments and associated volumes. As an example of this, small substitutions of Co with Fe in the $Co_{23}B_6$ structure are predicted to stabilize it even though $Co_{23}B_6$ and $Fe_{23}B_6$ are not predicted to be stable. Negative ΔE values were obtained for compositions ranging between $Co_{21}Fe_2B_6$ and $Co_{19}Fe_4B_6$ even after accounting for the possibility of Fe and Co substitutions in the known stable binary (Fe, Co) -B and (Fe, Co) -Zr phases in the stoichiometries allowed by the primitive cells of these structures. For a more comprehensive investigation of this issue, large supercells allowing for a better approximation to complete solid solubility in the competing phases would be required.

VII. CONCLUSIONS

We have performed a theoretical investigation of the magnetic properties and stability of two closely related but

distinct structures of 23:6 stoichiometry. A detailed comparison between the theoretical calculations and experimental results for the Co-Zr binary system was described to provide justification for the theoretical method employed here. The compositions $(\text{Fe,Co,Ni})_{23}\text{Zr}_6$ and $(\text{Fe,Co,Ni})_{23}\text{B}_6$ were then chosen for detailed investigation because of the relevance to recent work in soft magnetic nanocomposite alloys in which these phases have been observed as secondary and even primary crystallization products.

The Fe-based phases are predicted to have the highest magnetizations while the magnetization of the Ni-based phases is predicted to be strongly or even completely suppressed. For the binary systems, the Co-based 23:6 structures of both prototypes are calculated to be the most stable. A strong tendency for the Zr incorporations to preferentially occupy the 8c site and stabilize the metastable $(\text{Fe,Co,Ni})_{23}\text{B}_6$ structures has been identified in agreement with previous theoretical calculations and experimental results. In contrast, B additions to the $(\text{Fe,Co,Ni})_{23}\text{Zr}_6$ structures appear to destabilize them and a much weaker site preference for B occupation would be expected. The predictions of these calculations appear to be in good agreement with qualitative experimental observations regarding factors which tend to stabilize the 23:6 structures during crystallization of (Fe,Co,Ni)-Zr-B-type metallic glasses currently available in the literature.

APPENDIX: BINARY (Fe, Ni)-Zr AND (Co, Fe, Ni)-B SYSTEMS

In this appendix, a brief comparison between the calculation results and experimental phase diagrams for the relevant binary systems not discussed in detail in the text is presented. For the Fe-Zr system (Table VII), all of the low-temperature equilibrium phases from the experimental phase diagram are also calculated to be stable here with the exception of the $\text{Fe}_{23}\text{Zr}_6$ phase.

In the Ni-Zr system (Table VIII), a much larger number of low-temperature equilibrium phases are observed in both the experimental and theoretical phase diagrams. With the ex-

ception of the $\text{Ni}_{10}\text{Zr}_7$ phase of Pearson symbol oC68 and the $\text{Ni}_{21}\text{Zr}_8$ phase of Pearson symbol aP29, the experimentally stable low-temperature phases are predicted to be stable in agreement with the experimental phase diagram. While the $\text{Ni}_{10}\text{Zr}_7$ phase is calculated to be only slightly unstable, the disagreement between theory and experiment is quite dramatic for the $\text{Ni}_{21}\text{Zr}_8$ structure. We suspect that the disagreement is due to incorrect structure information for the $\text{Ni}_{21}\text{Zr}_8$ phase as listed in the Pearson's Handbook of Crystal Data for Intermetallic Phases¹⁷ due to small Ni-Ni and Ni-Zr distances.

In the Fe-B system (Table IX), the agreement between the experimental phase diagram and the theoretical predictions of VASP is quite good. All of the low-temperature equilibrium phases from the experimental phase diagram are also predicted to be stable here. This system was discussed at length by Mihalkovic and Widom.¹⁴

In the Co-B system (Table X), a significant discrepancy exists between the phases calculated to be stable using the VASP program and the phases listed as the equilibrium phases at low temperatures on the equilibrium phase diagram. In particular, while the Co_3B , Co_2B (Pearson symbol tI12), and CoB (Pearson Symbol oP8) phases have all been reported as equilibrium phases at low temperature based on experimental phase diagrams, only the CoB phase is actually calculated to lie on the convex hull. Further experimental and theoretical study is needed to reduce these disagreements.

In the Ni-B system (Table XI), reasonable agreement between theory and experiment is observed as well. The only major discrepancy observed is the NiB phase of Pearson symbol oC8 which is not predicted to be stable based on the calculations performed here. In addition, the two Ni_4B_3 phases of Pearson symbols oP28 and mC28 are actually listed as slightly different compositions experimentally, both of which are included as equilibrium phases at low temperatures. For the calculations employed here, a perfect 4:3 stoichiometry is assumed and hence the oP28 structure is predicted to be low-temperature stable while the mC28 structure is predicted to be metastable.

TABLE VII. Experimentally stable phases of Fe-Zr included in the calculations throughout this work. Notice that the phases predicted to be theoretically stable at low temperatures are highlighted in gray.

Fe-Zr Experimentally Stable Phases						
Phase	(at % Zr)	Pearson	Prototype	$E_c(\text{ev/atom})$	$\Delta H_{\text{mix}}(\text{kJ/mol})$	$\Delta E(\text{meV/atom})$
BCC Fe	0 to 0.05	cI2	W	-8.205	0.00	0.0
$\text{Fe}_{23}\text{Zr}_6$	~20.7	cF116	$\text{Mn}_{23}\text{Th}_6$	-8.430	-16.65	7.9
Fe_2Zr	27.1 to 34	cF24	Cu_2Mg	-8.581	-28.07	-120.2
FeZr_3	75	oC16	Re_3B	-8.544	-14.34	-23.8
BCC Zr	93.5 to 100	cI2	W	-8.385	7.04	73.1
HCP Zr	99.7 to 100	hP2	Mg	-8.458	0.00	0.0

Stable at High Temperature						
FeZr_2	66.7 to 69	tI12	Al_2Cu	-8.540	-16.07	10.6

TABLE VIII. Experimentally stable phases of Ni-Zr included in the calculations throughout this work. Notice that the phases predicted to be theoretically stable at low temperatures are highlighted in gray.

Ni-Zr Experimentally Stable Phases						
Phase	(at % Zr)	Pearson	Prototype	$E_c(\text{ev/atom})$	$\Delta H_{\text{mix}}(\text{kJ/mol})$	$\Delta E(\text{meV/atom})$
FCC Ni	0 to 1.78	cF4	Cu	-5.458	0.00	0.0
Ni₅Zr	14.9 to 18.4	cF116	AuBe ₅	-6.294	-32.33	-2.4
Ni₇Zr₂	22.22	mC36	Ni ₇ Zr ₂	-6.569	-42.80	-10.7
Ni₃Zr	24.5 to 26.0	hP8	Ni ₃ Sn	-6.691	-46.49	-33.6
Ni₂₁Zr₈	27.6	aP29	Ni ₂₁ Hf ₈	-6.584	-28.65	184.8
Ni₁₀Zr₇	41.1 to 43.5	oC68		-7.17	-45.91	3
NiZr	50	oC8	CrB	-7.436	-46.04	-49.4
NiZr₂	66.7	tI12	Al ₂ Cu	-7.796	-32.54	-19.1
BCC Zr	97.1 to 100	cI2	W	-8.385	7.04	73.1
HCP Zr	99.8 to 100	hP2	Mg	-8.458	0.00	0.0

Stable at High Temperature

Ni₁₁Zr₉	45	tI40		-7.217	-39.39	70.1
--------------------------------------	----	------	--	--------	--------	------

Metastable or Unstable

Ni₂₃Zr₆	~20.7	cF116	Mn ₂₃ Th ₆	-6.449	-35.70	43.9
--------------------------------------	-------	-------	----------------------------------	--------	--------	------

TABLE IX. Experimentally stable phases of B-Fe included in the calculations throughout this work. Notice that the phases predicted to be theoretically stable at low temperatures are highlighted in gray.

B-Fe Experimentally Stable Phases						
Phase	(at % B)	Pearson	Prototype	$E_c(\text{ev/atom})$	$\Delta H_{\text{mix}}(\text{kJ/mol})$	$\Delta E(\text{meV/atom})$
BCC Fe	~0	cI2	W	-8.205	0.00	0.0
Fe₂B	33.3	tI12	Al ₂ Cu	-8.004	-29.45	-38.9
FeB	50 to 50.5	oP8	FeB	-7.810	-35.12	-135.3
B	100	hR12	α B	-6.686	0.00	0.0
B	100	hR105	β B	-6.652	3.30	34.1

Metastable or Stable in Some References

Fe₃B	25	oP16	Fe ₃ C	-8.043	-21.00	11.3
Fe₃B	25	tI32	Fe ₃ P	-8.038	-20.54	16.0

Metastable

Fe₂₃B₆	~20.7	cF116	Cr ₂₃ C ₆	-8.062	-16.49	18.6
-------------------------------------	-------	-------	---------------------------------	--------	--------	------

TABLE X. Experimentally stable phases of B-Co included in the calculations throughout this work. Notice that the phases predicted to be theoretically stable at low temperatures are highlighted in gray.

B-Co Experimentally Stable Phases						
Phase	(at % B)	Pearson	Prototype	$E_c(\text{ev/atom})$	$\Delta H_{\text{mix}}(\text{kJ/mol})$	$\Delta E(\text{meV/atom})$
FCC Co	~0	cF4	Cu	-6.990	20.50	20.5
HCP Co	~0	hP2	Mg	-7.010	0.00	0.0
Co₂₃B₆	~20.7	cF116	Cr ₂₃ C ₆	-7.095	-14.63	9.1
Co₃B	25	oP16	Fe ₃ C	-7.107	-17.13	16.8
Co₂B	33.3	tI12	Al ₂ Cu	-7.137	-22.62	24.6
CoB	50	oP8	FeB	-7.237	-37.48	-213.0
B	100	hR12	α B	-6.686	0.00	0.0
B	100	hR105	β B	-6.652	3.28	34.1

Metastable

Co₂₃B₆	~20.7	cF116	Cr ₂₃ C ₆	-7.095	-14.63	9.1
-------------------------------------	-------	-------	---------------------------------	--------	--------	-----

TABLE XI. Experimentally stable phases of B-Ni included in the calculations throughout this work. Notice that the phases predicted to be theoretically stable at low temperatures are highlighted in gray.

B-Ni Experimentally Stable Phases						
Phase	(at % B)	Pearson	Prototype	E_c (ev/atom)	ΔH_{mix} (kJ/mol)	ΔE (meV/atom)
FCC Ni	0 to 1.78	cF4	Cu	-5.458	0.00	0.0
Ni ₃ B	25	oP16	Fe ₃ C	-6.035	-25.93	-38.8
Ni ₂ B	33.3	tI12	Al ₂ Cu	-6.153	-27.47	-13.6
Ni ₄ B ₃	41.4	oP28		-6.259	-26.43	-2.7
Ni ₄ B ₃	43.6	mC28	Ni ₄ B ₃	-6.256	-26.16	2.7
NiB	50	oC8	CrB	-6.303	-22.19	9.7
B	100	hR12	α B	-6.686	0.00	0.0
B	100	hR105	β B	-6.652	3.30	34.1

Metastable or Unstable						
Ni ₂₃ B ₆	~20.7	cF116	Cr ₂₃ C ₆	-5.915	-19.47	20.7

*Corresponding author; pohodnic@andrew.cmu.edu

- ¹S. O. Y. Yoshizawa and K. Yamauchi, *J. Appl. Phys.* **64**, 6044 (1988).
- ²S. F. Y. Yoshizawa, D. H. Ping, M. Ohnuma, and K. Hono, *Mater. Sci. Eng., A* **375-377**, 207 (2004).
- ³A. Makino, K. Suzuki, A. Inoue, and T. Masumoto, *Mater. Trans., JIM* **32**, 551 (1991).
- ⁴M. A. Willard, J. H. Claassen, R. M. Stroud, and V. G. Harris, *J. Appl. Phys.* **91**, 8420 (2002).
- ⁵B. Idzikowski and A. Szajek, *Czech. J. Phys.* **54**, 59 (2004).
- ⁶M. A. Willard, T. M. Heil, and R. Goswami, *Metall. Mater. Trans. A* **38**, 725 (2007).
- ⁷P. R. Ohodnicki, S. Y. Park, H. K. McWilliams, K. Ramos, D. E. Laughlin, and M. E. McHenry, *J. Appl. Phys.* **101**, 09N108 (2007).
- ⁸J. Long, P. R. Ohodnicki, D. E. Laughlin, M. E. McHenry, T. Ohkubo, and K. Hono, *J. Appl. Phys.* **101**, 09N114 (2007).
- ⁹J. S. Blázquez, S. Lozano-Perez, and A. Conde, *Philos. Mag. Lett.* **82**, 409 (2002).
- ¹⁰A. Hsiao, Ph.D. thesis, Carnegie Mellon University, 2001.
- ¹¹Cohesive Energy Alloy Database, <http://alloy.phys.cmu.edu/>.
- ¹²P. E. Blochl, *Phys. Rev. B* **50**, 17953 (1994).
- ¹³G. Kresse and J. Furthmuller, *Phys. Rev. B* **54**, 11169 (1996).
- ¹⁴M. Mihalkovič and M. Widom, *Phys. Rev. B* **70**, 144107 (2004).
- ¹⁵*Binary Alloy Phase Diagrams*, 2nd ed. (ASM International, Materials Park, OH, 1990).
- ¹⁶*Phase Equilibria, Crystallographic and Thermodynamic Data of Binary Alloys*, Landolt-Börnstein, New Series, Group IV, Vol. 5, Pt. A-J (Springer, Berlin, Heidelberg, 1982).
- ¹⁷P. Villars and L. D. Calvert, *Pearson's Handbook of Crystallographic Data For Intermetallic Phases* (American Society for Metals, Metals Park, OH, 1985), Vols. 1 and 3.
- ¹⁸J. C. Gachon, M. Dirand, and J. Hertz, *J. Less-Common Met.* **85**, 1 (1982).
- ¹⁹K. H. J. Buschow, *J. Less-Common Met.* **85**, 221 (1982).
- ²⁰G. V. Ivanova, N. N. Shchegoleva, and A. M. Gabay, *J. Alloys Compd.* **432**, 135 (2006).
- ²¹R. C. O'Handley, *Modern Magnetic Materials: Principles and Applications* (Wiley, New York, 1999).
- ²²J. L. Finney, *Proc. R. Soc. London, Ser. A* **319**, 479 (1970).
- ²³D. Bagayoko and J. Callaway, *Phys. Rev. B* **28**, 5419 (1983).
- ²⁴K. Suzuki, A. Makino, A.-P. Tsai, A. Inoue, and T. Masumoto, *Mater. Sci. Eng., A* **179-180**, 501 (1994).
- ²⁵M. Widom and M. Mihalkovic, *J. Mater. Res.* **20**, 237 (2005).
- ²⁶Y. R. Zhang and R. V. Ramanujan, *J. Alloys Compd.* **403**, 197 (2005).
- ²⁷M. Kopcewicz, B. Idzikowski, and J. Kalinowska, *J. Appl. Phys.* **94**, 638 (2003).
- ²⁸H. Kimura, A. Inoue, Y. Murakami, and T. Masumoto, *Sci. Rep. Res. Inst. Tohoku Univ. A* **36**, 213 (1992).